Geomechanics and Engineering, *Vol. 39, No. 2 (2024) 157-170*
https://doi.org/10.12989/gae.2024.39.2.157

Study on acoustic emission fracture response and constitutive model of layered sandstone

Zhanping Song[1,2,3a], Xiaojing Xu[*1,2], Xiaoxu Tian[**1,2,3], Tong Wang[2,4b], Wanxue Song[1c] and Yun Cheng[2,5d]

[1]*School of Civil Engineering, Xi'an University of Architecture and Technology, Xi'an 710055, China*
[2]*Shaanxi Key Laboratory of Geotechnical and Underground Space Engineering, Xi'an 710055, China*
[3]*Institute of Tunnel and Underground Structure Engineering, Xi'an 710055, China*
[4]*School of Civil Engineering, Xi'an Shiyou University, Xi'an 710065, China*
[5]*College of Civil Engineering, Yancheng Institute of Technology, Yancheng 224051, China*

(*Received February 27, 2023, Revised September 18, 2024, Accepted September 30, 2024*)

Abstract. In the present study, the acoustic emission characteristics of hard sedimentary sandstone with varying bedding dip angles were examined through uniaxial compression tests using a rock mechanics creep apparatus combined with an acoustic emission system. The deformation and failure behavior of the sandstone was analyzed by correlating acoustic emission parameters with stress over time. A damage constitutive model was developed, incorporating cumulative acoustic emission ringing counts as a key parameter, with time acting as the intermediary. The findings indicate that, despite the differences in bedding dip angles, the stress-strain curves of the samples follow a similar pattern throughout the loading process, passing through four distinct phases: compaction, elastic deformation, yielding, and post-peak failure. The fracture patterns of the sandstone are influenced by the dip angle of the bedding. Acoustic emission parameters, including the ringing count, cumulative ringing count, and energy, align with these four stages of the stress-strain curve. During the compaction and elastic deformation phases, acoustic emissions remain in a quite state, with only brief spikes at points of rapid stress change. In the unstable fracture stage, acoustic emissions become highly active, while they return to a quite state in the post-fracture stage. The RA value of the acoustic emission displays a banded pattern as time progresses, with areas of dense clustering. When the stress curve declines, RA values enter an active period, mainly associated with the generation of shear cracks. Conversely, during periods of smooth stress progression, RA values remain in a quiet state, primarily linked to the formation of tensile cracks. The time-based damage constitutive model for layered sandstone effectively captures the entire process of rock fracture development.

Keywords: acoustic emission; bedding inclination; constitutive model; layered sandstone; rupture response

1. Introduction

The issue of floor heave deformation in tunnels constructed through layered sedimentary rock has become a significant concern for the long-term operation of high-speed railways (Cheng *et al.* 2024). Understanding the mechanical and acoustic properties of these layered rocks is crucial for guiding the construction, operation, and maintenance of tunnels in sedimentary rock formations (Cheng *et al.* 2019, Cheng *et al.* 2022, Wang *et al.* 2019).

Reviewing the literature indicates that numerous studies have focused on the mechanical characteristics of layered rocks, primarily concentrating on mechanical property tests and fundamental acoustic emission parameters (Wang *et al.* 2021, Meng *et al.* 2022, Mohammadi *et al.* 2019). In this context, acoustic emission, recognized as a mature, reliable, and non-destructive testing method (Carpinteri *et al.* 2007, Kim *et al.* 2019), has been widely employed to monitor the damage processes in materials such as metal, wood, concrete, and rock (Dai *et al.* 2018, Sirdesai *et al.* 2018, Liu *et al.* 2020, Gou *et al.* 2021). Chu *et al.* (2020) explored the effect of bedding dip angles on the mechanical properties and fracture modes of layered sandstone, linking their evolution to acoustic emission monitoring. Yang *et al.* (2016) investigated the spatial and temporal patterns of acoustic emission timing, box dimension, and energy release in rocks with varying dip angles, revealing the fracture mechanisms in layered rocks. Wang *et al.* (2020) employed uniaxial compression acoustic emission testing to examine cumulative energy, amplitude, and dominant signal frequency, identifying the key characteristics of frequency variation and energy distribution throughout the sandstone failure process. Su *et al.* (2011) conducted uniaxial and triaxial tests on sandstone, using acoustic emission to monitor rock failure behavior under different loading conditions. Li *et al.* (2014) combined resistivity measurements with acoustic emission techniques to study sandstone failure under uniaxial compression, developing a

*Corresponding author, Ph.D. Student
E-mail: xuxiaojing_789@163.com
**Corresponding author, Ph.D.
E-mail: tianxiaoxu@xauat.edu.cn
[a]Ph.D.
[b]Ph.D.
[c]Master
[d]Ph.D.

ISSN: 2005-307X (Print), 2092-6219 (Online)

damage evolution equation and introducing criteria and precursors for rock failure states. Wasantha *et al.* (2014) monitored energy release during the deformation of dry and water-saturated sandstone with varying dip angles using acoustic emission, concluding that energy release is higher in dry conditions, and decreases with increasing bedding dip angles. Song *et al.* (2021) analyzed prefabricated crack specimens at different angles using parameters like ringing count, acoustic emission energy, and RA value. Dou *et al.* (2021) examined the impact of different dip angles on sandstone failure, utilizing acoustic emission and scanning electron microscopy, and proposed that the turning points of acoustic emission signals and cumulative ringing counts could serve as indicators for predicting dynamic disasters in coal and rock masses. Wang *et al.* (2016) studied the effects of shale bedding on failure modes and acoustic emission behavior, offering insights for interpreting microseismic monitoring during field fracturing. Lv *et al.* (2022) conducted three-point bending tests and acoustic emission analysis on layered sandstone with varying dip angles. Their results demonstrated that failure strength, peak deformation, AE count, and damage rate, as reflected by AE count and RA-AF distribution, varied significantly with bedding dip angles. Establishing a quantitative relationship between acoustic emission parameters and mechanical properties, as well as predicting rock mass instability, remains a challenging yet vital area of study (Song *et al.* 2022a, Song *et al.* 2022b, Kim *et al.* 2013, Kim *et al.* 2015). Wu *et al.* (2015) developed a coupling relationship between acoustic emission ringing count, damage variables, and stress, providing a framework for rock damage assessment. Based on uniaxial compression tests, Yang *et al.* (2021) derived a constitutive damage model for sandstone, incorporating loading rate and cumulative acoustic emission ringing counts. Geng *et al.* (2017) examined acoustic emission behavior during concrete failure, qualitatively describing damage evolution through changes in acoustic emission energy and ringing times. Kong *et al.* (2016) used thermal damage parameters and cumulative acoustic emission counts to establish a coupling model for temperature-stress-acoustic emission behavior during high-temperature deformation and fracture of sandstone. Yang *et al.* (2018) defined rock damage variables through non-uniform deformation and derived statistical damage constitutive equations for uniaxial and triaxial compression scenarios, accounting for nonlinear elasticity and residual stress. Zhang *et al.* (2022) adapted a modified constitutive model based on AE rate process theory to fit the stress-strain curves of basalt fiber reinforced concrete (BFRC), finding that the model accurately described BFRC's mechanical behavior under dynamic splitting loads. The performed literature survey reveals that research on the mechanical response and damage evolution of hard sedimentary rock with pronounced bedding structures remains underdeveloped (Bahaaddini *et al.* 2013, Song *et al.* 2019, Song *et al.* 2020, Zhang *et al.* 2022). Therefore, investigating the acoustic emission response of hard sandstone with a layered structure and deriving an appropriate damage constitutive equation is of considerable importance.

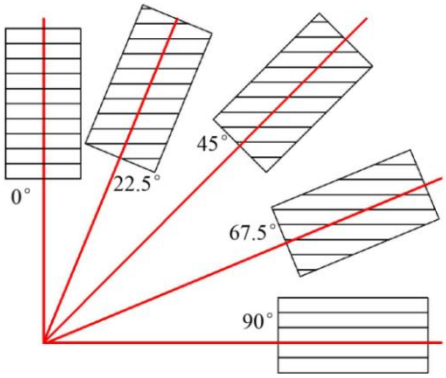

Fig. 1 Sandstone sample drilling direction diagram

Fig. 2 Standard sandstone samples with different bedding dip angles

This paper presents uniaxial compression acoustic emission tests on hard sedimentary sandstone with varying bedding dip angles, examining how changes in the dip angle affect the acoustic emission characteristics of the rock. Based on the findings, a damage constitutive model is developed, using cumulative acoustic emission ringing count as a key parameter and incorporating time as a medium. This model offers a theoretical framework for understanding the damage and failure processes in rock, providing valuable insights for analyzing the deformation stability of layered sandstone in engineering applications.

2. Test survey

2.1 Rock sample preparation

Hard sandstone with a uniaxial compressive strength exceeding 30 MPa was sourced from Chengdu, Sichuan Province. This sandstone features a naturally uniform bedding structure. For the experiment, rock blocks with consistent mineral distribution (indicated by no noticeable color variations), uniform bedding alignment, and no visible defects were selected. Based on the drilling orientation shown in Fig. 1, these rock blocks were cut and polished into sandstone samples with bedding dip angles of 0°, 22.5°, 45°, 67.5°, and 90°. Following the guidelines outlined in the "Engineering Rock Mass Test Method Standard" and the International Society for Rock Mechanics Standards, the samples were prepared with dimensions of

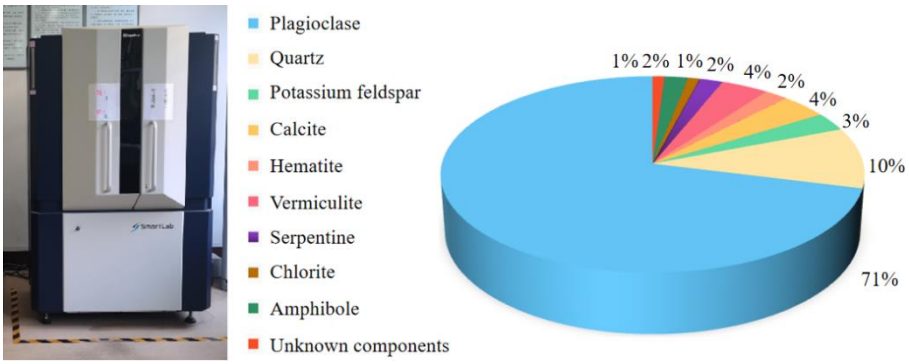

Fig. 3 Sandstone mineral content table

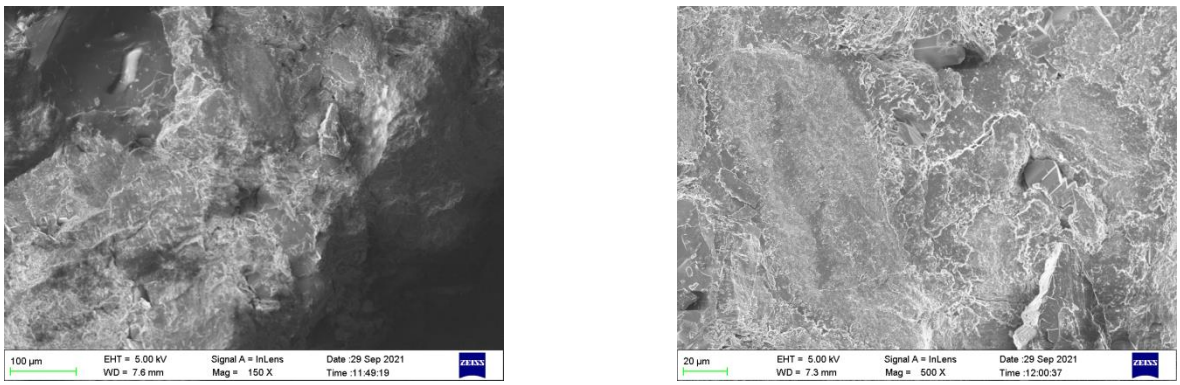

(a) 150 times microscopic scanning (b) 500 times microscopic scanning

Fig. 4 Microscopic scanning results of sandstone

100 mm in height and 50 mm in diameter, maintaining a height-to-diameter ratio of 2:1. The non-parallelism and non-perpendicularity of the end faces were kept within 0.02 mm, with a deviation of ± 0.001 mm. The prepared samples underwent weighing and density measurements, with any damaged or irregular samples being discarded. The finalized standard sandstone samples are depicted in Fig. 2. To assess the mineral composition and content, X-ray diffraction (XRD) analysis was conducted on the prepared standard specimens.

2.2 Mineral composition of rock samples

XRD analysis was performed on the prepared standard sandstone samples. The results revealed the mineral composition of the sandstone to be as follows: plagioclase (71%), quartz (10%), potassium feldspar (3%), calcite (4%), hematite (2%), vermiculite (4%), serpentine (2%), chlorite (1%), amphibole (2%), and unknown components (1%). The XRD diffraction pattern and mineral content distribution are illustrated in Fig. 3. Microstructural scanning of the sandstone residual samples, at magnifications of 150x and 500x, is shown in Fig. 4. The scans indicate that the sandstone exhibits a high degree of homogeneity with uniformly distributed pores. The pore development shows localized connectivity without any discernible flaky or layered characteristics. The crystals are densely packed, though the cement material between them is loosely arranged in a flocculent pattern. This variation in the elastic-plastic deformation properties is identified as the underlying cause of potential cracks within the sandstone. The flocculent distribution of the cement is accompanied by microcracks, while the crystal surfaces remain smooth and crack-free. However, distinct boundary cracks between the cement and crystals are present. These features arise from the sedimentary characteristics, which lead to slight variations in mineral morphology and distribution, primarily reflected in differences in mineral species, crystal size and arrangement, cement thickness, density, and the degree of cementation between crystals and cement. These variations are key contributors to the degradation of the mechanical properties and anisotropy of the sandstone, which are responsible for the development of a micro-layered structure.

2.3 Test equipment and programmes

A rock mechanics creep instrument (WAW-600, Xi'an Lichuang Company, China) was used in this study to perform uniaxial compression tests. This equipment can provide a maximum axial force of 600 kN, with an effective measurement range between 20 kN and 600 kN. The disturbance frequency of the system ranges from 0 to 3 Hz. The device was paired with an acoustic emission system (SAEU2S-1016-4, Beijing Shenghua Company, China) to simultaneously monitor the stress-strain behavior and acoustic emission characteristics during the deformation of the rock samples.

The acoustic emission equipment had a signal acquisition threshold of 40 dB, with a maximum data

Table 1 Uniaxial compression test scheme of bedding sandstone

Rock number	Mass/g	dry density/g·mm^{-3}	bedding dip/°	loading rate/MPa·s^{-1}
0-2	487.7	2.49×10^{-3}	0.0	1.5
0-1	486.1	2.48×10^{-3}	0.0	1.5
22.5-6	485.8	2.48×10^{-3}	22.5	1.5
22.5-8	487.3	2.48×10^{-3}	22.5	1.5
45-4	482.8	2.46×10^{-3}	45.0	1.5
45-8	485.2	2.47×10^{-3}	45.0	1.5
67.5-4	483.8	2.47×10^{-3}	67.5	1.5
67.5-18	476.1	2.43×10^{-3}	67.5	1.5
90-4	478.9	2.44×10^{-3}	90.0	1.5
90-8	484.3	2.47×10^{-3}	90.0	1.5

acquisition frequency of up to 10 MHz. Moreover, it had a 16-bit accuracy and a maximum data pass rate of 30 MB/s, with a peak impact count rate of 400 K/s. Additionally, the system could automatically filter out any interference from the collected waveform signals, ensuring a clean dataset. The time interval for data acquisition was set to 400 μs, and the acquisition frequency was configured at 1000 kHz.

2.4 Test scheme

To investigate the impact of varying bedding dip angles on the mechanical properties and acoustic emission characteristics of sandstone, samples with dip angles of 0°, 22.5°, 45°, 67.5°, and 90° were subjected to weighing, density measurement, and X-ray diffraction analysis. The results revealed that the sandstone mass ranged from 476.1 to 487.7 g, while the density fell between 2.43×10^{-3} g/mm^3 and 2.49×10^{-3} g/mm^3. The qualified sandstone samples were categorized into five groups, based on their dip angles, with each group containing two samples, amounting to a total of 10 samples. The grouping details are presented in Table 1.

3. Test survey

The uniaxial compressive stress-strain curves for the layered sandstone samples with different bedding dip angles are illustrated in Fig. 5. It is observed that the stress-strain curves for all the specimens, regardless of bedding dip angle, exhibit a similar pattern during the loading process. The process can be divided into four distinct stages: the compaction stage (OA), elastic stage (AB), yield stage (BC), and post-peak failure stage (CD).

At the beginning of stress loading, the OA section of the curve shows a concave upward trend, where the maximum stress for all the specimens in the compaction stage reaches 10 MPa. As the bedding dip angle increases, the curvature of the concave section becomes more pronounced, indicating a slow initial increase in stress followed by a more rapid rise. This effect is particularly noticeable in the samples with bedding dip angles of 67.5° and 90°, where a distinct concave inflection point can be observed. Once the compaction stage concludes, the internal voids within the rock diminish, transitioning the rock into the elastic deformation stage, where the stress-strain curve follows a near-linear growth. It is also found that as the applied load further increases, the rock progresses into the stable expansion and deformation phase of microcracks. During this phase, small cracks appear on the specimen's surface, occasionally accompanied by cracking sounds, as the deformation curve slightly decreases, compressing the rock further. There is no clear correlation between the slope of the stress-strain curve and the bedding angle during the elastic deformation and microcrack expansion phases, although the maximum slope first decreases and then increases as the bedding dip angle rises. As the load continues to increase, the stress-strain curve reaches its peak strength. For specimens with smaller bedding dip angles (0°, 22.5°, and 45°), the stress-strain curve is relatively smooth, showing little fluctuation near the peak stress, resembling a unimodal curve. However, for larger dip angles (67.5° and 90°), the curve exhibits significant zigzag variations near the peak stress. This phenomenon occurs because, at smaller dip angles, the bedding has minimal influence on rock failure, resulting in predominantly brittle deformation. Conversely, at higher bedding angles, the bedding becomes a major factor in rock failure, promoting sliding along the bedding planes under load, which leads to more pronounced fluctuations in the stress-strain curves. As the load continues beyond the peak, macroscopic cracks begin to intersect and penetrate through the rock, leading to significant fracturing along the main fracture plane, although the rock sample remains largely intact. The stress-strain curve then drops sharply; however, instead of a complete post-fracture drop, a rebound in the curve is observed. This rebound phenomenon is particularly noticeable in samples with bedding dip angles of 22.5°, 45°, and 90°

Fig. 5 reveals that the anisotropy of sandstone significantly influences the fracture modes of the rock. When the bedding dip angle of the sandstone is 0°, the rock exhibits typical X-type conjugate shear cracks and monoclinic shear cracks, both of which are fully penetrated. Due to the inherent inhomogeneity of the rock, some tensile cracks are present. However, the rock primarily undergoes shear failure when the bedding dip angle is 0°, as the dominant failure mode. At a dip angle of 22.5°, the rock surface presents incompletely penetrating X-type conjugate shear cracks. A fully penetrating monoclinic shear crack also develops, forming the main shear surface. This is accompanied by a small number of localized splitting cracks. Consequently, at a dip angle of 22.5°, shear failure remains the dominant failure mechanism. When the dip angle is increased to 45°, the failure mode becomes more complex. The rock mass on the surface separates from the central core, with a middle fracture occurring on the rock surface. Additionally, ejection failure at the top and bottom of the rock, as well as a through-going main fracture surface in the core, are observed. This failure mode is characterized by a combination of shear and tensile (splitting) failures. At a bedding dip angle of 67.5°, two distinct main shear planes appear along the bedding direction. Fine mesh-like cracks develop at the bottom of the rock, accompanied by localized

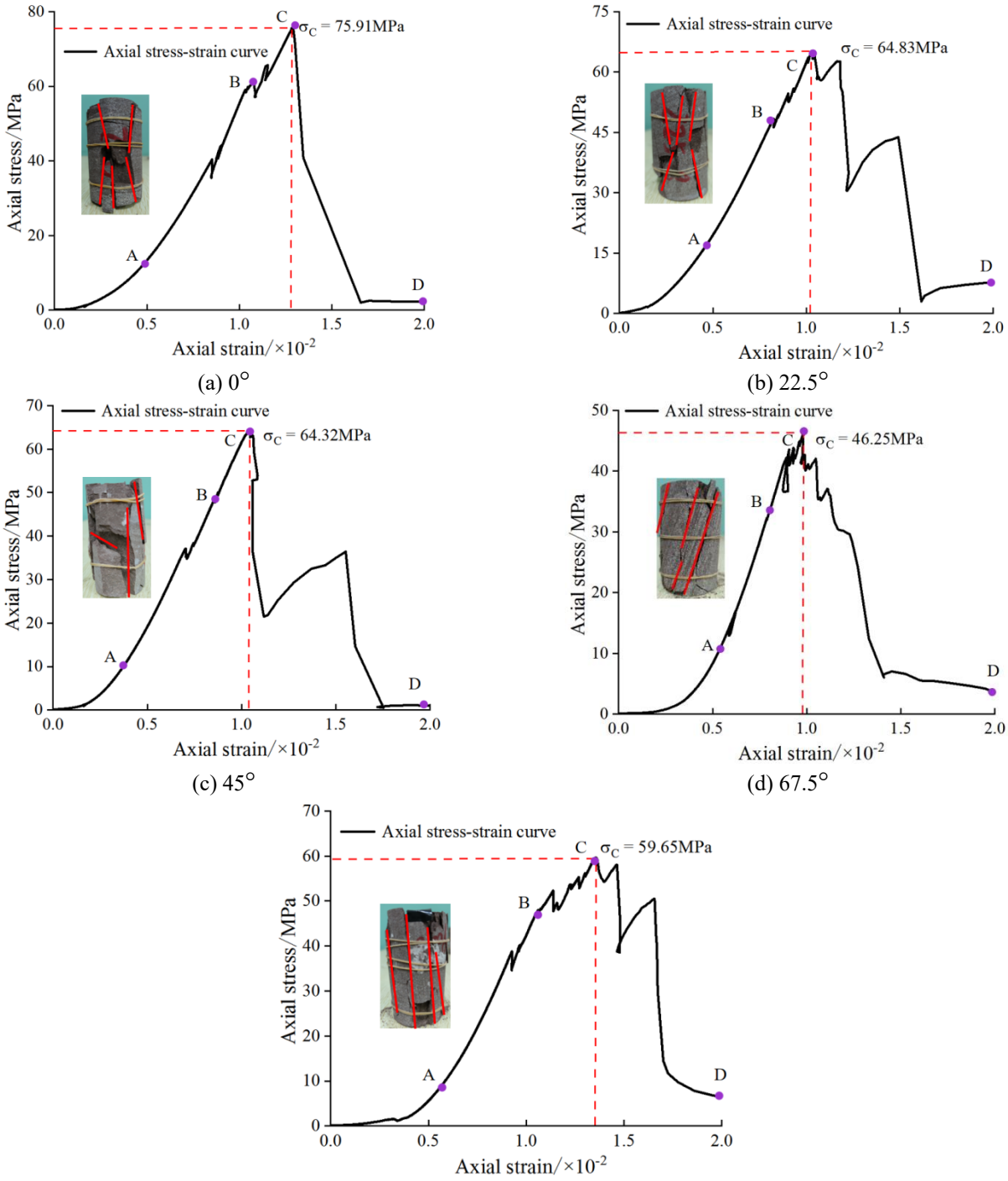

Fig. 5 Uniaxial compression stress-strain curves of sandstone with different dip angles

ejection failure. The rock slips along the bedding plane, aligning closely with the strength failure plane angle of 45° ± φ/2 as described by the Mohr-Coulomb theory. At this dip angle, the rock primarily undergoes shear slip failure. When the bedding dip angle reaches 90°, multiple vertical cracks penetrate from the bottom to the top of the rock. The resulting fragments are predominantly thin strips, indicative of splitting failure (a type of tensile failure). Additionally, a few localized fracture cracks are observed, but the primary failure mode is splitting.

4. Analysis of acoustic emission characteristics

To analyze the influence of acoustic emission (AE) characteristics during rock failure, Figs. 6-8 present the relationship between AE ringing count, AE energy, RA value, stress, and time for various bedding dip angles.

4.1 Ring count and cumulative ring count

Fig. 6 illustrates the distribution characteristics of stress,

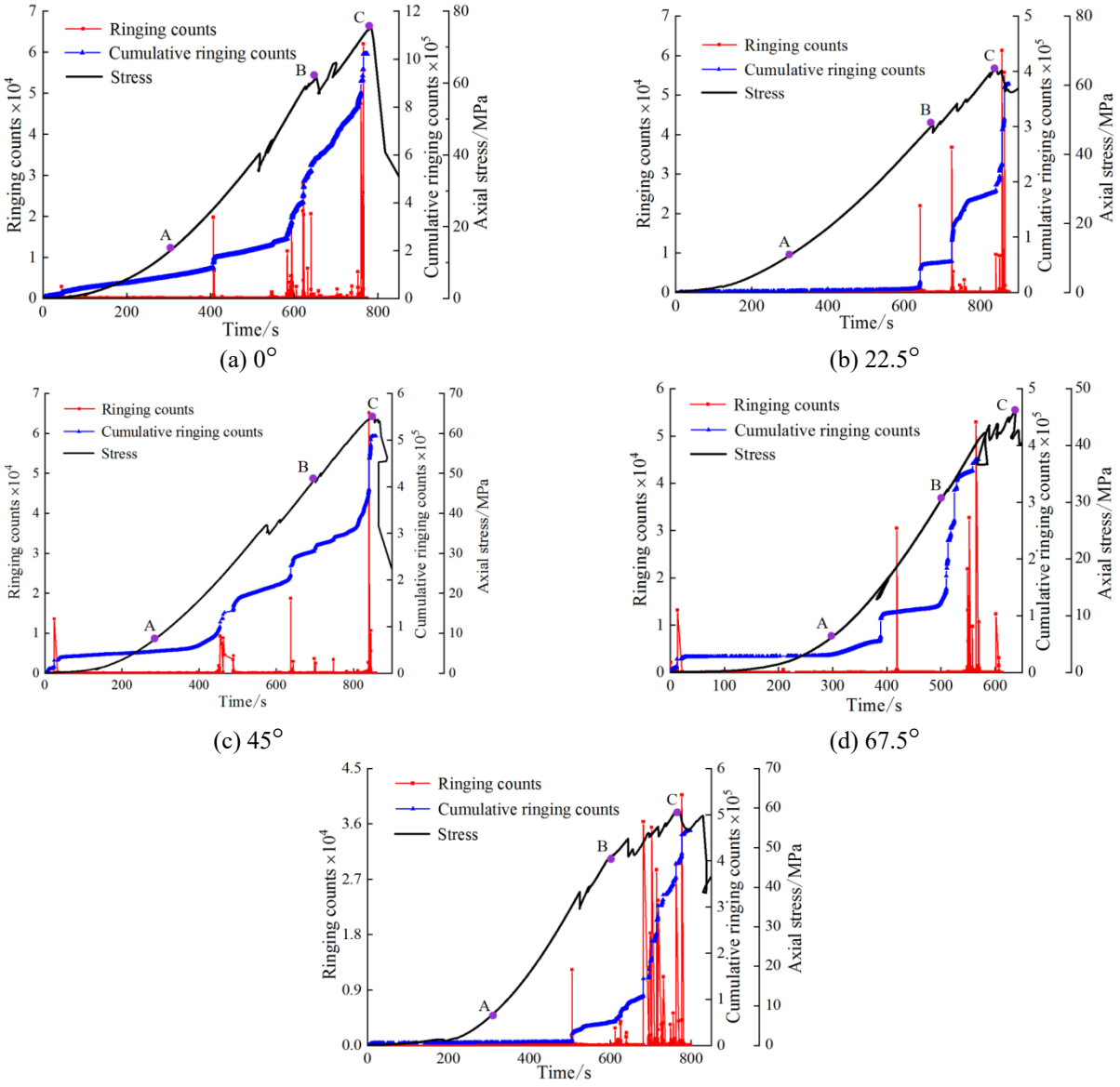

Fig. 6 Acoustic emission ringing count and cumulative ringing count-strain relationship diagram of sandstone with differen t dip angles

AE ringing count, cumulative ringing count, and time for layered sandstone with different bedding dip angles. A comparative analysis reveals a consistent correspondence between the stress and AE ringing count. During the compaction stage of the rock (denoted as OA), the AE ringing count is extremely low, and the cumulative ringing count increases very slowly, with an almost negligible slope. This period marks the "quiet phase" of AE activity. The reason behind this is that, in this stage, the rock's deformation is primarily limited to the compression and closure of internal voids and pre-existing cracks. There is no formation or propagation of new cracks, thus resulting in minimal acoustic emission activity.

As the rock transitions into the elastic deformation stage (AB), the acoustic emission ringing count becomes more active, with a slight increase in count. Overall, AE activity remains relatively calm, though sudden spikes in the ringing count occur at specific points. These spikes correspond to abrupt changes in rock stress. The slope of the cumulative ringing count curve also increases compared to the compaction stage, and the curve experiences noticeable jumps where the ringing count surges, showing a step-like increase. This behavior is attributed to uneven stress distribution within the rock, where crack expansion or rock debris ejection leads to increased AE activity. When the rock reaches the unstable fracture deformation stage, the AE ringing count surges significantly, remaining highly active. The slope of the cumulative ringing count curve steepens sharply, shifting from steady growth to a sudden rise. The peak AE ringing count coincides with the maximum point on the rock's stress-strain curve, marking the critical moment when the main crack penetrates, and the rock experiences failure.

In the post-peak failure stage, the AE ringing count

Table 2 Acoustic emission ringing count and cumulative ringing count parameter table of sandstone with different dip angles

Inclination	Peak ringing count / $\times 10^4$	Cumulative ringing count / $\times 10^5$	Peak stress / MPa
0°	2.7875	10.2152	75.91
22.5°	6.1279	3.77368	64.83
45°	1.8807	5.08163	64.32
67.5°	3.0520	3.75393	46.25
90°	4.0738	4.66030	59.65

rapidly declines, while the cumulative ringing count reaches its maximum and stabilizes. At this point, the AE activity returns to the quiet phase, signaling the end of the active fracture process and the rock's overall failure.

Based on the data in Fig. 6, Table 2 highlights the quantitative relationship between the AE ringing count and cumulative ringing count at the peak points of sandstone with different bedding dip angles. It is observed that the maximum ringing count at the peak stress does not follow a clear numerical pattern. This irregularity may be attributed to the inherent heterogeneity of the rock and the randomness in crack formation. However, the trend of the cumulative ringing count aligns closely with the variation in peak stress, showing a pattern that first decreases and then increases. The maximum cumulative ringing count occurs at a bedding dip angle of 0°, while the minimum appears at 67.5°. Notably, the range of cumulative ringing count values is substantial, spanning from 3.75393×10^5 to 10.2152×10^5. Compared to the minimum cumulative ringing count, the maximum value represents an increase of approximately 172%.

4.2 AE energy curve

Fig. 7 shows the evolution of AE energy over time for layered sandstone at different bedding dip angles. It is observed that there are both similarities and differences in the evolution of AE energy compared to the ringing count curve.

In the early stages of loading, including the compaction and linear deformation stages, the AE energy remains low, marking a quiet phase in development. Only brief surges in energy are detected where local stress drops occur, which may be attributed to the initiation and progression of cracks in the sandstone. As time progresses and stress approaches its maximum value, the AE energy also increases, entering an active phase. During this period, the frequency of high-energy points rises, and AE energy reaches its peak near the maximum stress. While AE energy typically reaches its maximum near the peak stress for dip angles of 0°, 22.5°, 67.5°, and 90°, the behavior is notably different for a 45° inclination angle. At this angle, the maximum AE energy is 12.785×10^5 mV·μs at 446 seconds, significantly higher than the AE energy at the point of maximum stress (858 seconds), where it reaches only 5.0393×10^5 mV·μs. The AE energy at 446 seconds is 2.5 times greater than at 858 seconds. This anomaly can be interpreted by the fact that, at an inclination of 45°, a significant spalling event occurs at the bottom of the specimen during loading (as shown in Fig. 5(c)). The spalling fragments are large in volume and detach over a short period, leading to an instantaneous release of a large amount of energy. This accounts for the earlier peak in AE energy, which differs from the typical pattern seen at other inclination angles.

When the bedding inclination angle is small (0°, 22.5°, 45°), the acoustic emission energy exhibits 2-3 distinct active stages. Specifically, when the inclination angle is 0°, the AE energy active stages occur at 390–410 s, 600–700 s, and 800–820 s. When the inclination angle is 22.5°, the active stages are observed at 620–750 s and 830–870 s. When the inclination angle is 45°, the active stages occur at 430–500 s, 630–750 s, and 820–830 s. In these cases, the AE energy displays an overall pattern of alternating quiet and active phases, which can be described as quiet-active (short duration)-quiet-more active (long duration)-quiet-most active (short duration). Furthermore, the AE energy near the point of maximum stress tends to be concentrated within a short timeframe, typically lasting 20-40 s. This behavior is primarily due to local cracks first forming on the rock's surface when subjected to force, triggering the first active energy phase.

As external force continues to increase, old cracks grow while new cracks form, resulting in the second active phase of energy. With further loading, the cracks propagate rapidly, leading to rock failure and the third energy surge. Conversely, for larger bedding dip angles (67.5° and 90°), the AE energy is characterized by one long, continuous active phase, which occurs near the maximum stress. The active period of AE energy in these cases is extended, lasting approximately 60–100 s. Before this prolonged active period, the AE energy displays a brief surge at points where stress decreases, following the pattern of calm-transient active-quiet-continuous active. The difference in behavior at larger dip angles is due to the fact that as force is applied, initial local cracks form, causing a short-term energy surge, similar to what is observed at smaller angles. However, as the load approaches the maximum stress, numerous fine cracks develop along the bedding. These cracks progressively grow and ultimately lead to slip failure along the bedding direction. The generation and expansion of fine cracks consume substantial energy, resulting in a prolonged active AE phase. Notably, at dip angles of 67.5° and 90°, the AE energy evolution curve exhibits a clear quiet period just before the rock fractures, which provides a valuable early warning signal for predicting rock failure.

The previous analysis of acoustic emission energy in rocks over time did not explore the precise quantitative relationships. To address this, Table 3 summarizes the peak acoustic emission energy and its timing for sandstone samples with varying bedding angles, as shown in Fig. 7.

Table 3 reveals that the time required from the start of loading to rock failure spans approximately 10 to 15 minutes (613.300 to 907.145 seconds). The duration of the loading phase initially decreases and then increases as the bedding angle of the sandstone rises. Specifically, the shortest loading period of 613.300 seconds occurs at a

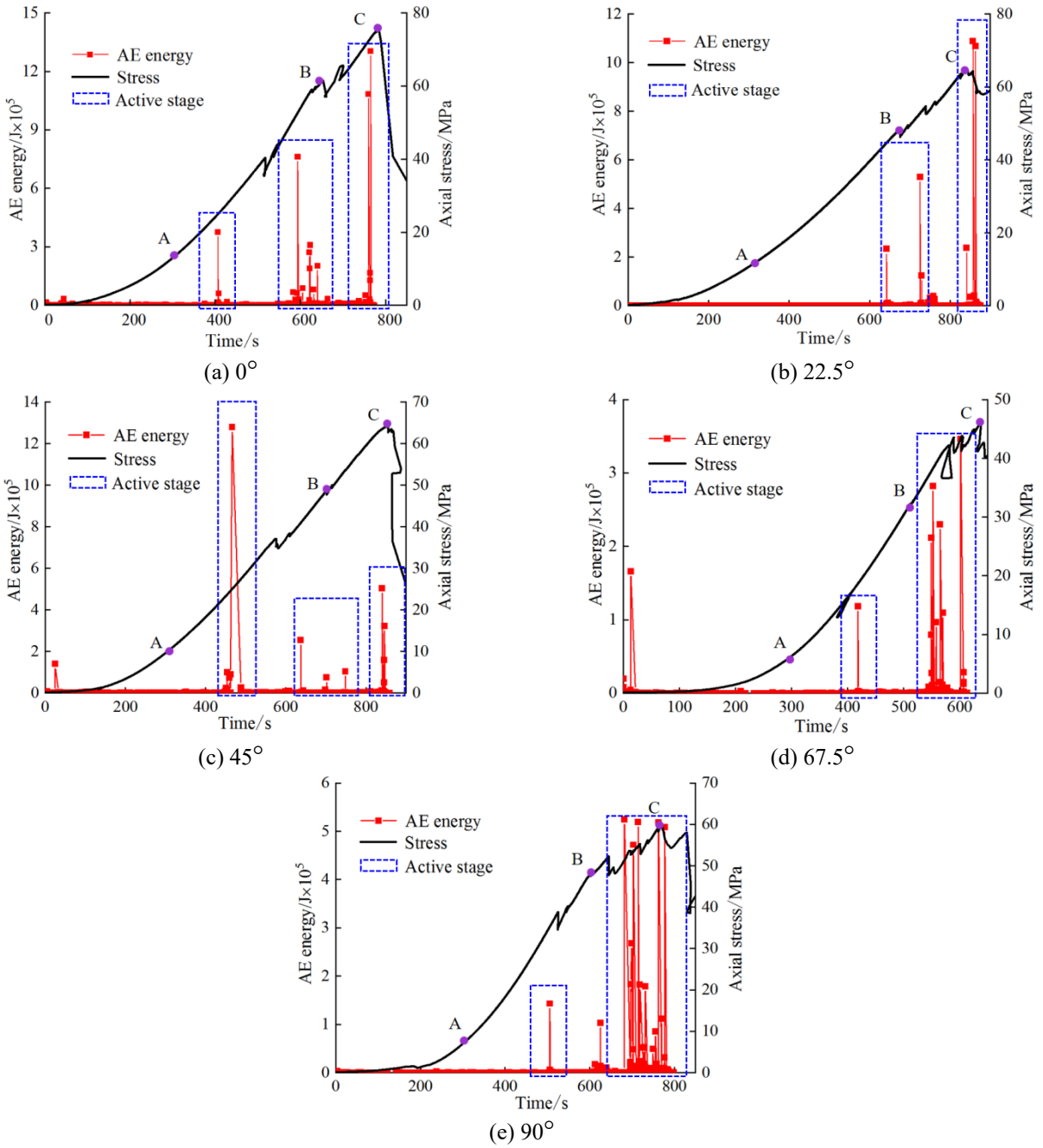

Fig. 7 Energy distribution map of sandstone with different dip angles

bedding angle of 67.5°. moreover, the longest loading period of 907.145 seconds is observed at a bedding angle of 0°. The difference between the longest and shortest loading times is 293.845 seconds. For bedding angles of 0°, 22.5°, 45°, and 90°, the loading durations are relatively similar, with a notable reduction only at 67.5°. Compared to the 67.5° angle, the loading times at 0°, 22.5°, 45°, and 90° are extended by 48%, 43%, and 30%, respectively. The 67.5° angle represents the most challenging condition for sandstone stability. In terms of peak acoustic emission energy, there is an initial decrease followed by an increase as the bedding angle changes. The lowest peak energy of 3.4616×10^5 mv·us is recorded at a 67.5° bedding angle, while the highest peak energy of 10.8848×10^6 mv·us is found at a 22.5° angle. This pattern in peak energy is consistent with the trends observed in peak stress, reflecting the underlying fracture characteristics of the rock.

Table 3 Peak energy timetable of sandstone with different dip angles

Bedding dip angle	Peak energy/mv·us	Duration/s	Peak stress/MPa
0°	13.0372×10^5	907.145	75.91
22.5°	10.8848×10^6	875.755	64.83
45°	5.0393×10^5	858.863	64.32
67.5°	3.4616×10^5	613.300	46.25
90°	5.0875×10^5	798.487	59.65

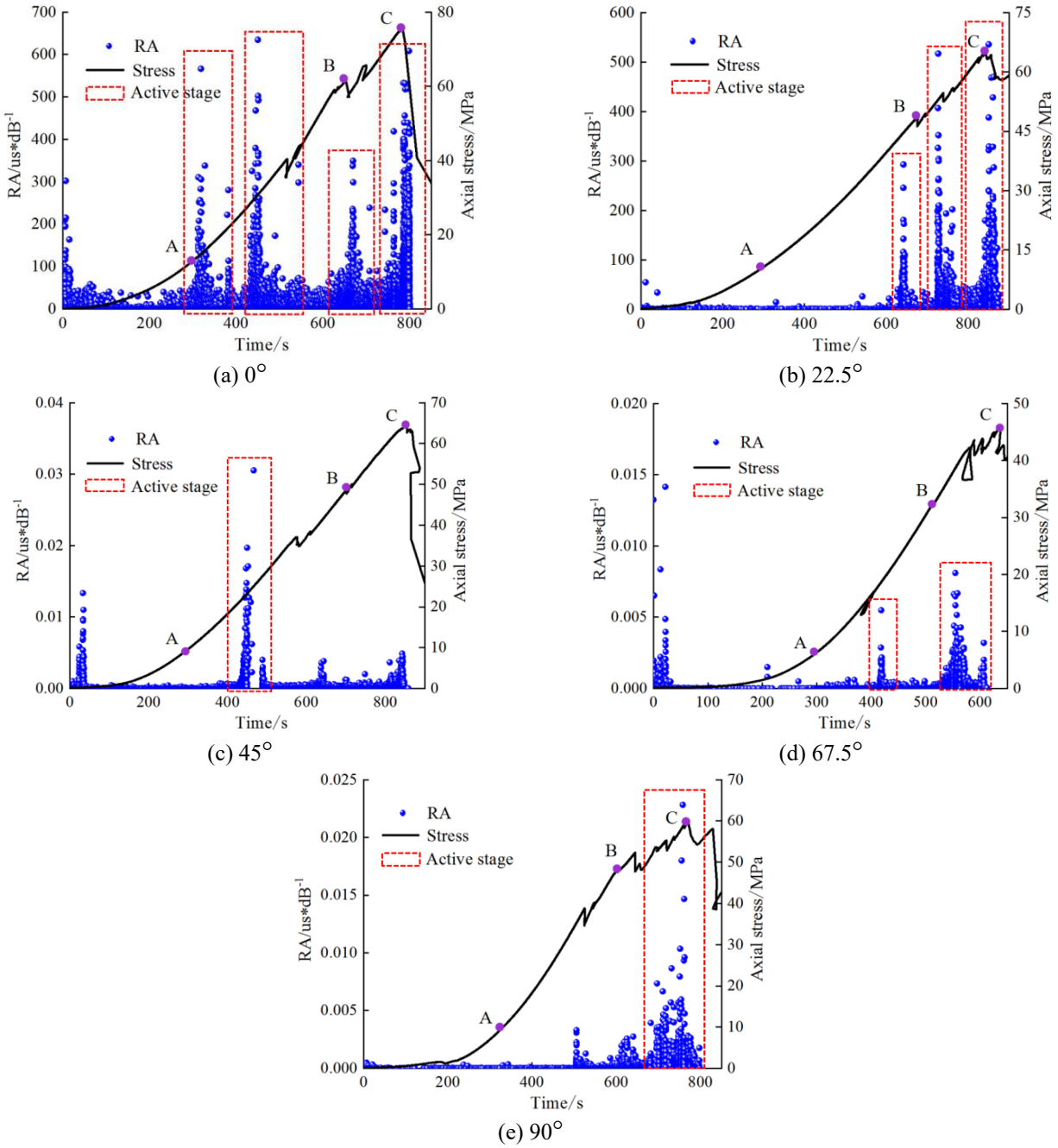

Fig. 8 Stress-RA-time distribution characteristics of sandstone with different bedding dip angles

4.3 AE energy curve

Fig. 8 illustrates the relationship between stress, RA, and time for sandstone samples with varying bedding dip angles. The RA values display a banded distribution over time, with notable density in specific areas. When the stress curve drops, RA values increase significantly, leading to a concentration of RA points. Conversely, when the stress curve remains stable, RA values are lower, and RA points are more spread out. The areas with high RA values are termed the "active periods," while those with low RA values are referred to as "quiet periods".

Fig. 8 reveals that samples with bedding angles of 0° and 22.5° exhibit multiple active periods characterized byhigh RA values, with peaks reaching 620 us·dB^{-1} and 500us·dB^{-1}, respectively. This high RA indicates extensive crack development, predominantly shear cracks, and typical X-type conjugate shear failure in sandstone at these angles. In contrast, at bedding angles of 45°, 67.5°, and 90°, the RA active periods are less pronounced, with maximum RA values of 0.032 us·dB^{-1}, 0.015 us·dB^{-1}, and 0.022 us·dB^{-1}, respectively. These lower RA values suggest fewer shear cracks, and the rock primarily experiences tensile fractures. As the bedding angle increases, the failure mode of the sandstone transitions from shear-dominated failure to a combination of shear and tensile failure.

Table 4 Ringing time-cumulative ringing count fitting parameters

Bedding dip angle	Fitting parameter C	Fitting parameter D	Correlation coefficient R^2
0°	1840.06	0.00411	0.98
22.5°	442.55	0.00744	0.85
45°	820.72	0.00550	0.89
67.5°	914.84	0.00992	0.92
90°	97.30	0.0108	0.98

5. Analysis of acoustic emission characteristics

To analyze the impact of acoustic emission characteristics during rock failure, Figs. 6-8 depict the relationship between AE ringing count, AE energy, RA, and stress over time for different bedding angles.

5.1 Acoustic emission cumulative ringing count and time fitting

Previous studies by Xie *et al.* (2021) and Yang *et al.* (2021) have indicated that the cumulative ringing count of acoustic emissions can be described by an exponential function of time. The trends shown in Fig. 6 demonstrate that the cumulative ringing count and the duration of loading for sandstone samples with various bedding angles align with this exponential trend. However, Xie *et al.* (2021) presented a model where the cumulative ringing count does not equal zero at time zero, which does not accurately reflect the observed data. On the other hand, Yang *et al.* (2021) incorporated loading rate effects into their model, which diverges from the focus of this study. Thus, building on the work of both studies, this paper proposes the following equation to describe the relationship:

$$N = C \cdot \left[\exp(Dt) - 1 \right] \tag{1}$$

where C and D are fitting parameters; n is the cumulative ringing count; t is the duration.

The data presented in this paper are fitted using Eq. (1) to fit the time-cumulative ringing count. The results of this fitting process are illustrated in Fig. 9 and summarized in Table 4.

Fig. 9 and Table 4 demonstrate that the fitting curve closely aligns with the test curve, demonstrating a correlation coefficient ranging from 0.85 to 0.98. This indicates that the time-cumulative ringing count function established is effective. However, noticeable fluctuations in the cumulative ringing count over time suggest significant crack expansions in the specimen during these periods. The fitted curve remains relatively smooth, implying that Eq. (1) does not capture the fracture sensitivity as accurately as the test curve. To address this, the functional relationship between strain and cumulative ringing count has been derived by combining the time-strain relationship.

$$\varepsilon = A \cdot In\left[B \cdot In\left(N/C + 1 \right) / D + 1 \right] \tag{2}$$

5.2 Establishment of acoustic emission damage constitutive equation

According to Lemaitre's equivalent strain theory, the stress of rock in a non-destructive state multiplied by a damage factor can effectively represent the stress of rock under damage conditions. This relationship can be mathematically expressed as follows

$$\sigma = \sigma'\left(1 - D\right) = E\varepsilon\left(1 - D\right) \tag{3}$$

where σ is nominal stress; σ' is the effective stress; d is the damage variable; E is elastic modulus; ε is strain.

Assuming that the micro-element strength of rock follows a Weibull distribution, the damage factor D is

$$D = 1 - \exp\left[-(\frac{\varepsilon}{\alpha})^m \right] \tag{4}$$

Yang *et al*. (2021) derived the relationship between the parameter m and α based on the statistical damage model

$$\begin{cases} m = \dfrac{1}{In\left(E\varepsilon_c / \sigma_c \right)} \\ \left(\dfrac{\varepsilon_c}{\alpha} \right)^m = \dfrac{1}{m} \end{cases} \tag{5}$$

where ε_c is the peak strain; σ_c is the peak stress.

Substitute Eq. (4) into Eq. (3) yields the following expression:

$$\sigma = E\varepsilon\left[\exp\left(-(\frac{\varepsilon}{\alpha})^m \right) \right] \tag{6}$$

Substituting the cumulative ringing count relationship from Eq. (2) into Eq. (6) to derive the damage factor based on acoustic emission yields the following expression:

$$D = 1 - \exp\left[-(\frac{A \cdot In\left[B \cdot In\left(N/C + 1 \right) / D + 1 \right]}{\alpha})^m \right] \tag{7}$$

Then the damage factor Eq. (7) is substituted into Eq. (6), and the damage constitutive model based on acoustic emission is obtained:

$$\sigma = E\varepsilon\left[1 - \exp\left(-(\frac{A \cdot In\left[B \cdot In\left(N/C + 1 \right) / D + 1 \right]}{\alpha})^m \right) \right] \tag{8}$$

5.3 Verification of damage constitutive model

Using time as the intermediary, the cumulative ringing count from acoustic emissions and strain data are incorporated into the damage constitutive model to develop a model parameterized by cumulative ringing count. To assess the validity and accuracy of this model, the fundamental parameters are derived from the previously collected test data, as detailed in Table 5. These parameters are then applied to Eq. (8), allowing for the creation of a

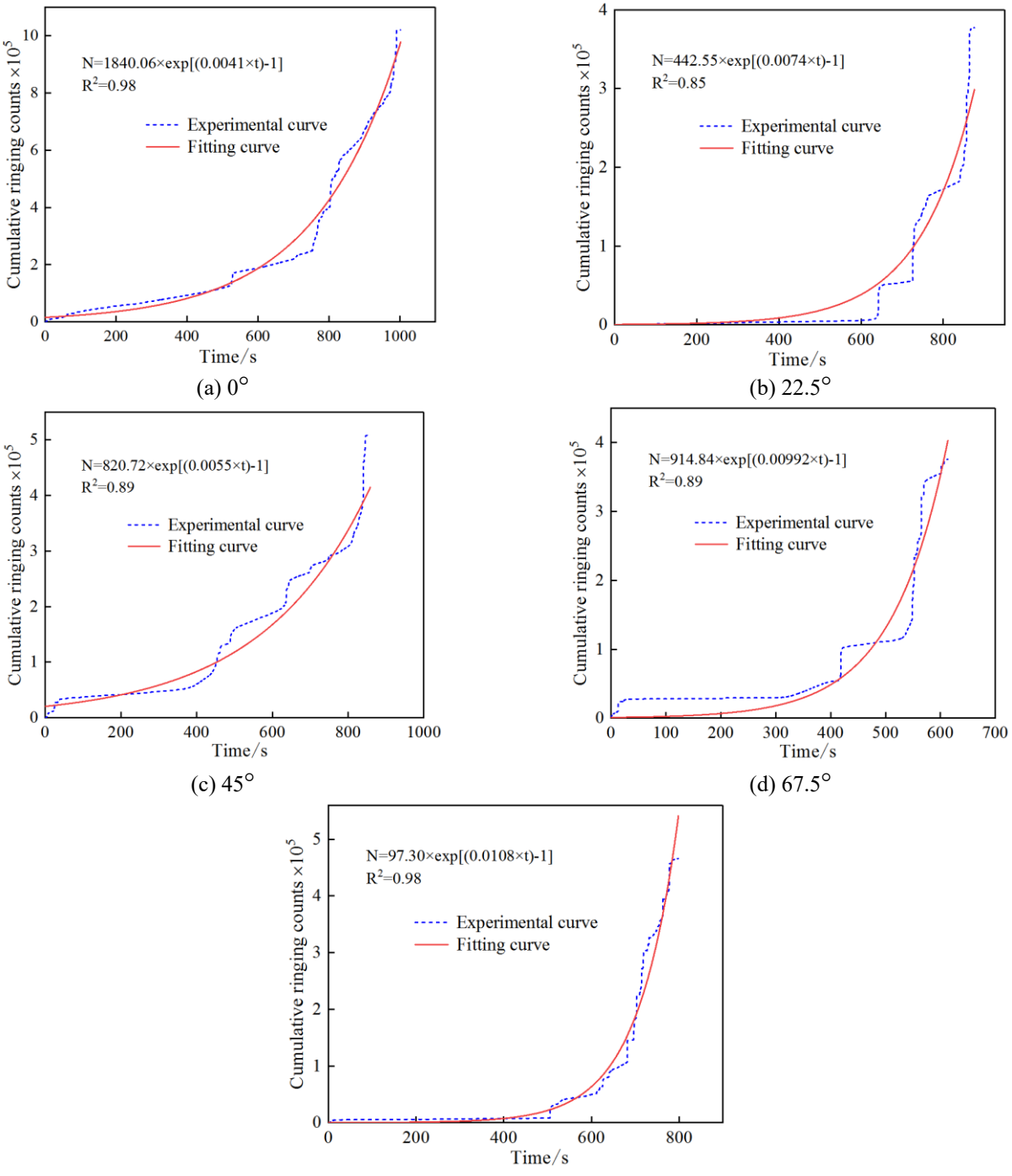

Fig. 9 Time-cumulative ringing count test curve and fitting curve

Table 5 Parameters of acoustic emission damage constitutive model

Bedding dip angle	*A*	*B*	*C*	*D*	*m*	*α*
0°	0.56	0.0075	1840.06	0.00411	7.58	0.0168
22.5°	0.51	0.0067	442.55	0.00744	3.71	0.0146
45°	0.49	0.0075	820.72	0.00550	3.70	0.0149
67.5°	0.21	0.1096	914.84	0.00992	2.48	0.0141
90°	0.37	0.028	97.30	0.0108	2.78	0.0196

curve that illustrates the relationship between cumulative ringing count and strain, as depicted in Fig. 10.

Fig. 10 reveals that the model curve aligns well with the theoretical curve for bedding angles of 0°, 22.5°, and 90°. While the fit is less precise for angles of 45° and 67.5°, the overall trend remains consistent, demonstrating the applicability of the proposed constitutive model. However, the test curves exhibit significant fluctuations due to ringing count surges from rock fractures, capturing the fracture response characteristics of the rock. In contrast, the model curve is smoother, highlighting a limitation in the model as

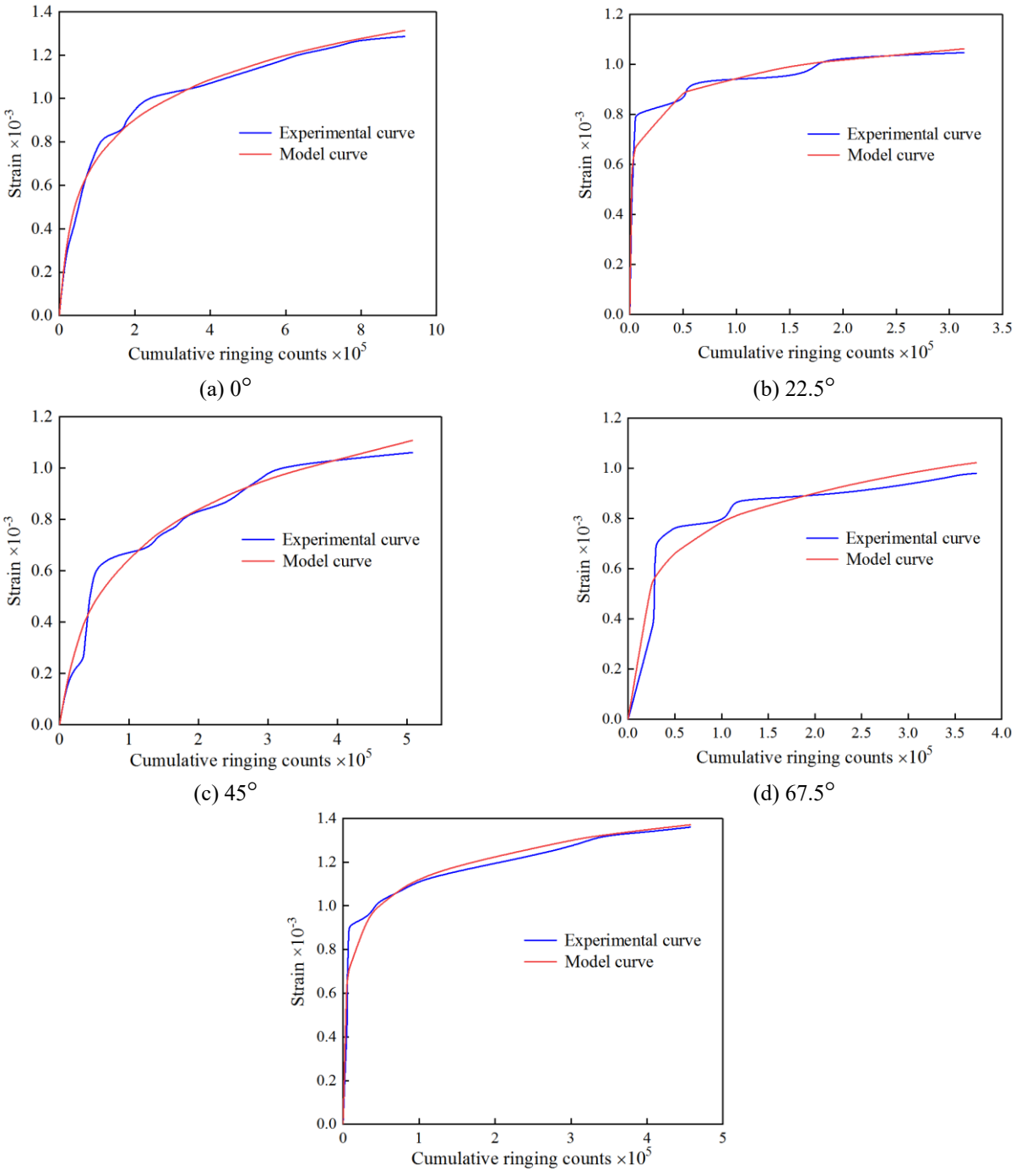

Fig. 10 Accumulative ring count-strain curves of different bedding dip angles

it may omit some fracture details. The effectiveness of the model depends on the appropriateness of the selected time-strain and time-cumulative ringing count fitting equations; an inadequate fitting equation can significantly reduce the model's applicability.

6. Conclusions

This study investigated the acoustic emission (AE) characteristics and constitutive models of hard sedimentary sandstones with distinct bedding structures under uniaxial compression tests. The main achievements of this article can be summarized as follows:

• For smaller bedding angles (0°, 22.5°, 45°), the stress-strain curves of the sandstones generally follow a single-peak pattern. However, for larger bedding angles (67.5°, 90°), the curves display a zigzag pattern before reaching the peak. Both the peak stress and peak strain initially decrease and then increase as the bedding angle rises. As the bedding dip angle grows, the failure modes transition from pure

shear failure to a combination of shear and tension failure, then to shear slip failure, and eventually to splitting failure.

• The AE curves are strongly correlated with the stress-strain curves. Fluctuations in the stress-strain curves are associated with surges in AE ring counts, cumulative ring counts, and energy. The AE RA values show a banded distribution over time, with distinct regions of high and low density. At bedding angles of 0° and 22.5°, multiple active periods with high RA values are observed, mainly indicating shear failure. In contrast, at 45°, 67.5°, and 90°, fewer active RA periods are detected, suggesting a shift towards combined tension-shear failure mechanisms.

• By fitting cumulative AE ring counts against time and linking these to strain through time, a damage constitutive model parameterized by AE ring counts was developed. The comparison between the model's predictions and the experimental results confirms the validity and accuracy of the proposed constitutive model.

Acknowledgments

The authors deeply appreciate support from the National Natural Science Foundation(52178393) and the Science and Technology Innovation Team of Shaanxi Innovation Capability Support Plan (Grant No. 2020TD005).

References

Bahaaddini, M., Sharrock, G. and Hebblewhite, B.K. (2013), "Numerical investigation of the effect of joint geometrical parameters on the mechanical properties of a non-persistent jointed rock mass under uniaxial compression", *Comput. Geotech.*, **49**(2013), 206-225. https://doi.org/10.1016/j.compgeo.2012.10.012.

Carpinteri, A., Lacidogna, G. and Pugno, N. (2007), "Structural damage diagnosis and life-time assessment by acoustic emission monitoring", *Eng. Fract. Mech.*, **74**(1-2), 273-289. https://doi.org/10.1016/j.engfracmech.2006.01.036.

Cheng, Y., Song, Z.P., Liu, Z., Tian X., Qian, W., Lu, X. and Yang, T. (2024), "Micro-cracking morphology and dynamic fracturing mechanism of natural brittle sandstone containing layer structure under compression", *Constr. Build. Mater.*, **425**(2024)136051. https://doi.org/10.1016/j.conbuildmat.2024.136051.

Cheng, Y., Song, Z.P., Song, W.X., Li, S.G., Yang, T.T., Zhang, Z.K., Wang, T., and Wang, K.S. (2021), "Strain performance and fracture response characteristics of hard rock under cyclic loading", *Geomech. Eng.*, **26**(6), 551-563. https://doi.org/10.12989/gae.2021.26.6.551.

Cheng, Y., Song, Z.P., Yang, T.T., Han, J.J., Wang, B.W. and Zhang, Z.K. (2022), " Investigating the aging damage evolution characteristics of layered hard sandstone using digital image correlation", *Constr. Build. Mater.*, **353**(2022), 128838. https://doi.org/10.1016/j.conbuildmat.2022.128838.

Chu, C.Q., Wu, S.C., Zhang, S.H., Guo, P. and Zhang, M. (2020), "Mechanical behavior anisotropy and fracture characteristics of bedded sandstone", *J. Central South Univ.* (*Science and Technology*), **51**(8), 2232-2246. https://doi.org/10.11817/j.issn.1672-7207.2020.08.018.

Dai, Q.L., Ng, K., Zhou, J., Kreiger, E.L. and Ahlborn, T.M. (2012), "Damage investigation of single-edge notched beam tests with normal strength concrete and ultra high performance concrete specimens using acoustic emission techniques", *Constr. Build. Mater.*, **31**(2012), 231-242. https://doi.org/10.1016/j.conbuildmat.2011.12.080.

Dou, L.T., Yang, K. and Chi, X.L. (2021), "Fracture behavior and acoustic emission characteristics of sandstone samples with inclined precracks", *Int. J. Coal Sci. Technol.*, **8**(1), 77-87. https://doi.org/10.1007/s40789-020-00344-x.

Geng, J.S., Sun, Q., Zhang, Y.C., Cao, L.W. and Zhang, W.Q. (2017), "Studying the dynamic damage failure of concrete based on acoustic emission", *Constr. Build. Mater.*, **149**(2017), 9-16. https://doi.org/10.1016/j.conbuildmat.2017.05.054.

Gou, P., Wu, S.C., Zhang, G. nd Chu, C.Q. (2021), "Effects of thermally-induced cracks on acoustic emission characteristics of granite under tensile conditions", *Int. J. Rock Mech. Min. Sci.*, **144**(2021), 104820. https://doi.org/10.1016/j.ijrmms.2021.104820.

Kim, J.S., Lee, K.S., Cho, W.J., Choi, H.J. and Cho, G.C. (2013), "A combined method of Wigner-Ville distribution with a theoretical model for acoustic emission source location in a dispersive media", *KSCE J. Civil Eng.*, **17**(6), 1284-1292. https://doi.org/10.1007/s12205-013-0418-6.

Kim, J.S., Lee, K.S., Cho, W.J., Choi, H.J. and Cho, G.C. (2015), "A comparative evaluation of stress-strain and acoustic emission methods for quantitative damage assessment of brittle rock", *Rock Mech. Rock Eng.*, **48**(2), 495-508. https://doi.org/10.1007/s00603-014-0590-0.

Kim, J.S., Kim, G.Y., Baik, M.H. and Cho, G.C. (2019), "A new approach for quantitative damage assessment of in-situ rock mass by acoustic emission", *Geomech. Eng.*, **18**(1), 11-20. https://doi.org/10.12989/gae.2019.18.1.011.

Kong, B., Wang, E.Y., Li, Z.H., Wang, X.R., Liu, J. and Li, N. (2016), "Fracture mechanical behavior of sandstone subjected to high-temperature treatment and its acoustic emission characteristics under uniaxial compression conditions", *Rock Mech. Rock Eng.*, **49**(12), 4911-4918. https://doi.org/10.1007/s00603-016-1011-3.

Li, S.C., Xu, X.J., Liu, Z.Y., Yang, W.M., Liu, B., Zhang, X., Wang, Z.C., Nie, L.C., Li, J.L. and Xu, L. (2014), "Electrical resistivity and acoustic emission response characteristics and damage evolution of sandstone during whole process of uniaxial compression", *Chinese J. Rock Mech. Eng.*, **33**(1), 1-23. https://doi.org/10.13722/j.cnki.jrme.2014.01.002.

Liu, Z., Yao, Q.G., Kong, B. and Yin, J.L. (2020), "Macro-micro mechanical properties of building sandstone under different thermal damage conditions and thermal stability evaluation using acoustic emission technology", *Constr. Build. Mater.*, **246**(2020), 118485. https://doi.org/10.1016/j.conbuildmat.2020.118485.

Lv, H., Peng, K., Shang, X.Y., Wang, Y.Q. and Liu, Z.P. (2022), "Experimental research on the mechanical and acoustic emission properties of layered sandstone during tensile failure", *Theor. Appl. Fract. Mech.*, ,**118**(2022), 103225. https://doi.org/10.1016/j.tafmec.2021.103225.

Meng, Q.B., Liu, J.F., Xie, L.X., Pu, H., Yang, Y.G., Huang, B.X. and Qian, W. (2022), "Experimental mechanical strength and deformation characteristics of deep damaged-fractured rock", *Bull. Eng. Geol. Environ*., **81**(32), 1-27. https://doi.org/10.1007/s10064-021-02529-3.

Mohammadi, H. and Pietruszczak, S. (2019), "Description of damage process in fractured rocks", *Bull. Eng. Geol. Environ*., **113**(2019), 295-302. https://doi.org/10.1016/j.ijrmms.2018.12.003.

Sirdesai, N.N., Gupta, T., Singh, T.N. and Ranjith, P.G. (2018), "Studying the acoustic emission response of an Indian monumental sandstone under varying temperatures and strains", *Constr. Build. Mater.*, **168**(2018), 346-361.

https://doi.org/10.1016/j.conbuildmat.2018.02.180.
Song, Y.M., Zhao, K.J. and Yang, X.B. (2021), "Study on AE characteristics of red sandstone samples with prefabricated crack under uniaxial compression", *J. Saf. Sci. Technol.*, **17**(11), 131-136. https://doi.org/10.11731/j.issn.1673-193x.2021.11.020.
Song, Z.P., Cheng, Y., Yang, T.T., Huo, R.K., Wang, J.B., Liu, X.R. and Zhou, G.N. (2019), "Analysis of compression failure and acoustic emission characteristics of limestone under permeability-stress coupling", *J. China Coal Soc.*, **44**(9), 2751-2759. https://doi.org/10.13225/j.cnki.jccs.018.1425.
Song, Z.P., Cheng, Y., Tian, X.X., Wang, J.B. and Yang, T.T. (2020), "Mechanical properties of limestone from Maixi tunnel under hydro-mechanical coupling", *Arabian J. Geosci.*, **13**(9), 1-11. https://doi.org/10.1007/s12517-020-05373-z.
Song, Z.P., Song, W.X., Cheng, Y., Yang, T.T., Wang, T. and Wang, K.S. (2022a), "Investigation on strain characteristics and fatigue constitutive model of limestone under osmotic pressure and cyclic disturbance coupling", *KSCE J. Civil Eng.*, **26**(4), 1740-1753. https://doi.org/10.1007/s12205-022-1416-3.
Song, Z.P., Wang, T., Wang, J.B., Xiao, K.H. and Yang, T.T. (2022b), "Uniaxial compression mechanical properties and damage constitutive model of limestone under osmotic pressure", *Int. J. Damage Mech.*, **31**(4), 557-581. https://doi.org/10.1177/10567895211045430.
Su, C.D., Zhai, X.X., Li, B.F. and Li, H.Q. (2011), "Experimental study of the characteristics of acoustic emission for sandstone specimens under uniaxial and triaxial compression tests", *J. Min. Saf. Eng.*, **28**(2), 225-230.
Wang, C.Y., Chang, X.K. and Du, X.Y. (2020), "Analysis on dominantt-frequency characteristics of acoustic emission in sandstone uniaxial compression failure", *Chinese J. Undergr. Sp. Eng.*, **16**(2), 451-462.
Wang, J., Xie, L.Z., Xie, H.P., Li, R., He, B., Li, C.B., Yang, Z.P. and Gao, C. (2016), "Effect of layer orientation on acoustic emission characteristics of anisotropic shale in Brazilian tests", *J. Nat. Gas Sci. Eng.*, **36**(2016), 1120-1129. https://doi.org/10.1016/j.jngse.2016.03.046.
Wang, T., Song, Z.P., Yang, J.Y., Wang, J.B. and Zhang, X.G. (2019), "Experimental research on dynamic response of red sandstone soil under impact loads", *Geomech. Eng.*, **17**(4), 393-403. https://doi.org/10.12989/gae.2019.17.4.393.
Wang, Y., Zhang, B., Li, B. and Li, C.H. (2021), "A strain-based fatigue damage model for naturally fractured marble subjected to freeze-thaw and uniaxial cyclic loads", *Int. J. Damage Mech.*, **30**(10), 1594-1616. https://doi.org/10.1177/10567895211021629.
Wasantha, P.L.P., Ranjith, P.G. and Shao, S.S. (2014), "Energy monitoring and analysis during deformation of bedded-sandtone: Use of acoustic emission", *Ultrasonics*, **54**(2014), 217-226. https://doi.org/10.1016/j.ultras.2013.06.015.
Wu, X.Z., Liu, J.W., Liu, X.X., Zhao, K. and Zhang, Y.B. (2015), "Study on the coupled relationship between AE accumulative ring-down count and damage constitutive model of rock", *J. Min. Saf. Eng.*, **32**(1), 28-34+41. https://doi.org/10.13545/j.cnki.jmse.2015.01.005.
Xie, Z.L., Yan, X.Q., Fu, M.F. and Fan, B.S. (2012), "Study on the coupled relationship between AE accumulative ring-down count and damage constitutive model of rock", *Appl. Acoust.*, **32**(6), 462-467.
Yang, S.Q. and Jing, H.W. (2013), "Evaluation on strength and deformation behavior of red sandstone under simple and complex loading paths", *Eng. Geol.*, **164**(2013), 1-17. https://doi.org/10.1016/j.enggeo.2013.06.010.
Yang, W.J., Xie, Q., Ban, Y.X., He, X.B. and Peng, G.Y. (2021), "The acoustic emission characteristics and damage constitutive model of sandstone under variable loading rates", *Chinese J. Undergr. Sp. Eng.*, **17**(1), 71-79.
Yang, X.B., Han, X.X., Liu, L.E., Zhang, Z.P. and Wang, X.Y. (2018), "Experimental study on the acoustic emission characteristics of non-uniform deformation evolution of granite under cyclic loading and unloading test", *Rock Soil Mech.*, **39**(8), 2732-2739. https://doi.org/10.16285/j.rsm.2018.0048.
Yang, Z.Q., Deng, W.X., Zhang, P.H., Wang, P.T., Zhang, T.W. and Yang, T.H. (2016), "The influence of bedding angle on acoustic emission characteristics in biotite granulite", *J. Min. Saf. Eng.*, **33**(3), 521-527. https://doi.org/10.13545/j.cnki.jmse.2016.03.022.
Zhang, H., Jin, C.J., Wang, L., Pan, L.Y., Liu, X.Y. and Ji, S.S. (2022), "Research on dynamic splitting damage characteristics and constitutive model of basalt fiber reinforced concrete based on acoustic emission", *Constr. Build. Mater.*, **319**(2022), 126018. https://doi.org/10.1016/j.conbuildmat.2021.126018.
Zhang, Z.K., Song, Z.P., Cheng, Y., Huo, R.K., Song, W.X., Wang, K.S., Wang, T., Yang, T.T. and Liu, W. (2022), "Acoustic emission characteristics and fracture response behavior of hard rock-like material under influence of loading rate", *Coal Geol. Explor.*, **44**(9), 2751-2759. https://doi.org/10.12363/issn.1001-1986.21.08.0418.

IC